Intrinsic structure of relaxor ferroelectrics from first principles

Xinyu Xu [1,2,*] Kehan Cai [3,*] Yubai Shi [4] Peichen Zhong [4] and Pinchen Xie [1,†]

[1]*Applied Mathematics and Computational Research Division, Lawrence Berkeley National Laboratory, Berkeley, California 94720, USA*

[2]*Department of Materials Science and Engineering, Stanford University, Stanford, California 94305, USA*

[3]*Department of Chemistry, Princeton University, Princeton, New Jersey 08544, USA*

[4]*Department of Materials Science and Engineering, National University of Singapore, Singapore*

(Received 23 November 2025; revised 27 March 2026; accepted 11 June 2026; published 6 July 2026)

We introduce FIRE-Swap, a first-principles-based framework for sampling representative compositional structures in complex perovskites using machine-learning interatomic potentials. By combining Monte Carlo chemical swaps with geometric relaxation, the method treats chemical and geometric degrees of freedom concurrently. Applied to lead magnesium niobate (PMN), lead zirconate titanate (PZT), and lead strontium titanate (PST), FIRE-Swap robustly predicts rock-salt-like chemical order in PMN, but not in the isovalent solid solutions PZT and PST with the same mixing ratio. For PMN, it further reveals anchored Nb clusters that host interconnected, noncoarsened polar nanoregions. These results provide a mesoscale structural basis for understanding relaxor ferroelectricity and establish FIRE-Swap as a practical route toward systematic, first-principles modeling of complex perovskites and related substitutionally disordered materials.

DOI: 10.1103/fz5h-1t5b

I. INTRODUCTION

Relaxor ferroelectrics, or relaxors, are glass-like crystals that respond strongly to electric fields over wide ranges of temperature and frequency [1–8]. Their hallmark is compositional disorder that disrupts the uniform ferroelectric distortion of conventional ferroelectrics [9]. Many relaxors are complex perovskites based on the ABO_3 structure, with mixed A- or B-site occupancy by multiple metallic species [see Fig. 1(a)]. The resulting compositional disorder implies random local fields and frustrated couplings, which can be described within a spin-glass framework [10], consistent with the phenomenological similarity between the permittivity peaks of relaxors and spin glasses [10,11]. However, spin-glass models assume homogeneous disorder and therefore miss intrinsic compositional structures (CS) in real materials, including short- and possibly long-range chemical order that can control macroscopic responses. Some complex perovskites, such as $Pb(Mg_{1/3}Nb_{2/3})O_3$, are heterovalent insulators in which charge, polar, and elastic degrees of freedom are strongly coupled, yielding a rugged energy landscape. This differs from metallic alloys, where screening and the absence of a polar lattice permit reduced lattice models [12] with simple effective interactions (e.g., Ising-type Hamiltonians). These differences motivate a first-principles framework that treats compositional and geometric relaxations concurrently [13].

Conventional first-principles approaches remain limited. Density functional theory (DFT) calculations are constrained to small supercells. Molecular dynamics (MD) and Monte Carlo (MC) simulations of atomistic models (effective Hamiltonians [14], all-atom force fields [15], etc.) can probe larger scales but rely on empirically chosen *Ansätze*, making accuracy difficult to assess or improve. Consequently, most studies assume *a priori* CS [16,17] for complex perovskites or optimize CS with semiquantitative models [18]. Experimental probes of CS are also limited [19–21]. For example, x-ray scattering reconstructs the averaged electron-density distribution, providing only statistical correlations of ionic distributions [19]. Annular dark-field scanning transmission electron microscopy (STEM) [22] can distinguish cations in real space, but projection effects and sample thickness obscure three-dimensional (3D) CS [20]. Reverse Monte Carlo fits to x-ray and neutron scattering data may reproduce average geometric statistics and infer 3D CS [21], but the accuracy of the morphological details of the refined CS is questionable because the mapping from scattering measurements to chemical order is subtle and nonunique (see Supplemental Material [23]).

To address this gap, we develop a first-principles framework that couples FIRE-Swap, a hybrid structure-sampling algorithm, with machine-learning interatomic potentials (MLIPs) to systematically determine intrinsic CS in complex perovskites. The framework is model-agnostic rather than tied to a specific MLIP architecture. In the following, we first introduce the algorithm and then demonstrate it using representative lead-based complex perovskites, including relaxor and nonrelaxor solid solutions.

*These authors contributed equally to this work.

†Contact author: pinchenxie@lbl.gov

Published by the American Physical Society under the terms of the Creative Commons Attribution 4.0 International license. Further distribution of this work must maintain attribution to the author(s) and the published article's title, journal citation, and DOI.

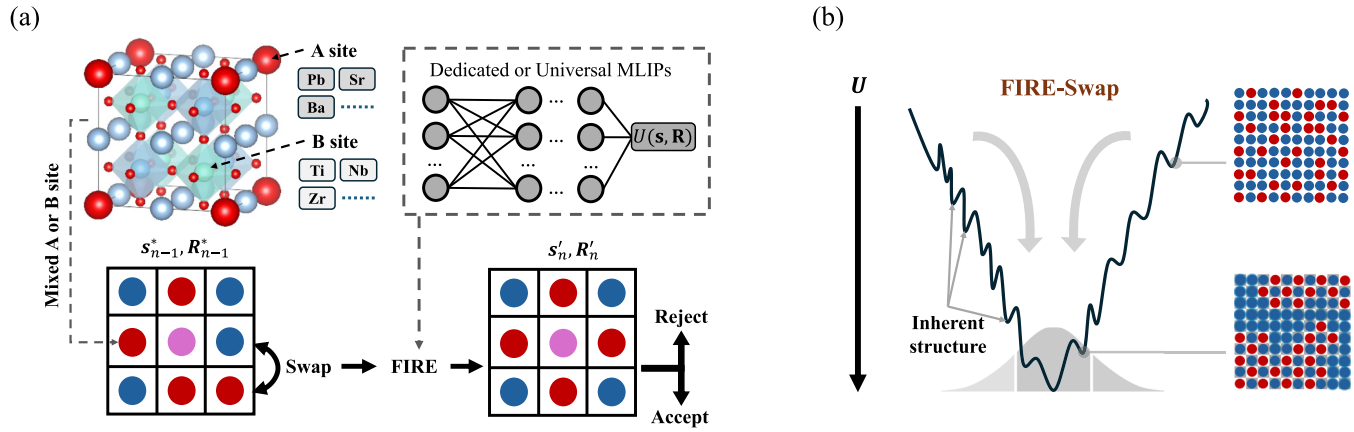


FIG. 1. (a) Sketch of a $3 \times 3 \times 3$ supercell of a complex perovskite and one iteration of the FIRE-Swap algorithm. (b) Schematic representation of the PES as a funnel. A FIRE-Swap simulation traverses the energy landscape and equilibrates to the Boltzmann distribution of inherent structures, illustrated as the gray distribution at the bottom. The two CS illustrations to the right of the PES represent a fully disordered state and a partially ordered state.

II. METHODS

Our approach requires MLIPs that represent the first-principles potential energy surface (PES) $U(\mathbf{s}, \mathbf{R})$, where $\mathbf{s} = (s_1, \ldots, s_N)$ and $\mathbf{R} = (\mathbf{r}_1, \ldots, \mathbf{r}_N)$ denote the species and positions of all N atoms in a periodic perovskite supercell. The MLIPs are trained on extensive DFT data that covers local compositional and geometric disorder, either for a single complex perovskite (dedicated MLIP) or across multiple complex perovskites (universal MLIP). Inspired by hybrid MD/MC methods for accelerated sampling [24–26], FIRE-Swap (see Fig. 1) uses an MLIP to alternate between (a) geometric optimization with the Fast Inertial Relaxation Engine (FIRE) algorithm [27] and (b) compositional relaxation via MC swapping of the chemical species of a random pair of target atoms, such as two A-site (or B-site) atoms in a complex perovskite with mixed occupancy.

Specifically, for the nth iteration, step (a) seeks the inherent structure $\mathbf{R}'_n = \text{argmin}_{\mathbf{R}} U(\mathbf{s}'_n, \mathbf{R})$ for a proposed new CS $\mathbf{s}'_n$ that differs from the previous CS $\mathbf{s}^*_{n-1}$. Step (b) computes the swap energy cost: $\Delta E_n = U(\mathbf{s}'_n, \mathbf{R}'_n) - U(\mathbf{s}^*_{n-1}, \mathbf{R}^*_{n-1})$. When $\Delta E_n < 0$, we accept the swap by setting $\mathbf{R}^*_n = \mathbf{R}'_n$ and $\mathbf{s}^*_n = \mathbf{s}'_n$. When $\Delta E_n > 0$, we accept the swap with probability $p = e^{-\Delta E_n / k_B T_{\text{FS}}}$, where T_{FS} is the sampling temperature. If rejected, we keep $\mathbf{R}^*_n = \mathbf{R}^*_{n-1}$ and $\mathbf{s}^*_n = \mathbf{s}^*_{n-1}$. We then propose a new configuration $\mathbf{s}'_{n+1}$ by swapping an arbitrary pair of target atoms that are nearest or next-nearest neighbors in $\mathbf{s}^*_n$. A neighborhood is defined by graph distance on the simple-cubic lattice. Each A site has six nearest and 12 next-nearest A-site neighbors. The same rule applies to B sites. The approach generalizes straightforwardly to systems with both mixed A-site and B-site occupancy.

Unlike hybrid MD/MC methods [24], which sample from a continuous distribution of atomic configurations, FIRE-Swap samples the equilibrium distribution p_{in} over the discrete set of inherent structures [local minima of the PES; see Fig. 1(b)] [28–30]. It is important to choose T_{FS} sufficiently below the melting temperature T_{M} so that p_{in} is concentrated on low-energy inherent structures, i.e., intrinsic structures. But T_{FS} should not be too low or the simulation may fail to escape midlying energy minima within a reasonable time, especially because the initial structure is typically high in energy. In practice, if the goal is to elucidate the CS of materials synthesized at high temperature and quenched without full equilibration, one may choose T_{FS} close to T_{M} to enhance the sampling of midlying CS favored by entropy.

III. RESULTS

A. Models

We apply FIRE-Swap to three lead-based complex perovskites: the relaxor $Pb(Mg_{1/3}Nb_{2/3})O_3$ (PMN) and the ferroelectric solid solutions $Pb(Zr_{1/3}Ti_{2/3})O_3$ (PZT) and $(Pb_{1/3}Sr_{2/3})TiO_3$ (PST) [31]. We use two density functionals, PBEsol [32] and SCAN [33], because they are among the best-performing GGA- and meta-GGA-level choices, respectively, for ferroelectric perovskites [34]. We then employ four MLIPs: a SCAN-based deep potential (DP) model [35–37], a SCAN-based Cartesian atomic cluster expansion long-range (CACE-LR) model [38–40], a PBEsol-based CACE-LR model, and a PBEsol-based UniPero model [41]. The DP and CACE-LR models are dedicated MLIPs that we trained for PMN, whereas UniPero is an existing universal MLIP for complex perovskites involving 14 metal elements and their solid solutions, including PMN, PZT, and PST [41]. The CACE-LR models include long-range electrostatic interactions, with latent Ewald summation [42]. The DP model is numerically more efficient than the others. All models achieve energy prediction errors on the order of 1 meV per atom on their respective test sets. Their training sets consist of small complex-perovskite supercells with different compositional and geometric disorder. Details are provided in Appendix A.

It is broadly accepted that PZT and PST lack significant chemical order, whereas the extent of chemical order in PMN remains debated [5,20,43–51]. Two models have dominated discussions of PMN CS. The first is the charge-balanced random-site model [47] (also known as the random-layer model), which involves two interpenetrating face-centered cubic sublattices [denoted β^{I} and β^{II}; see Fig. 2(a)] in the perovskite structure. In this model, B sites in β^{II} are occupied

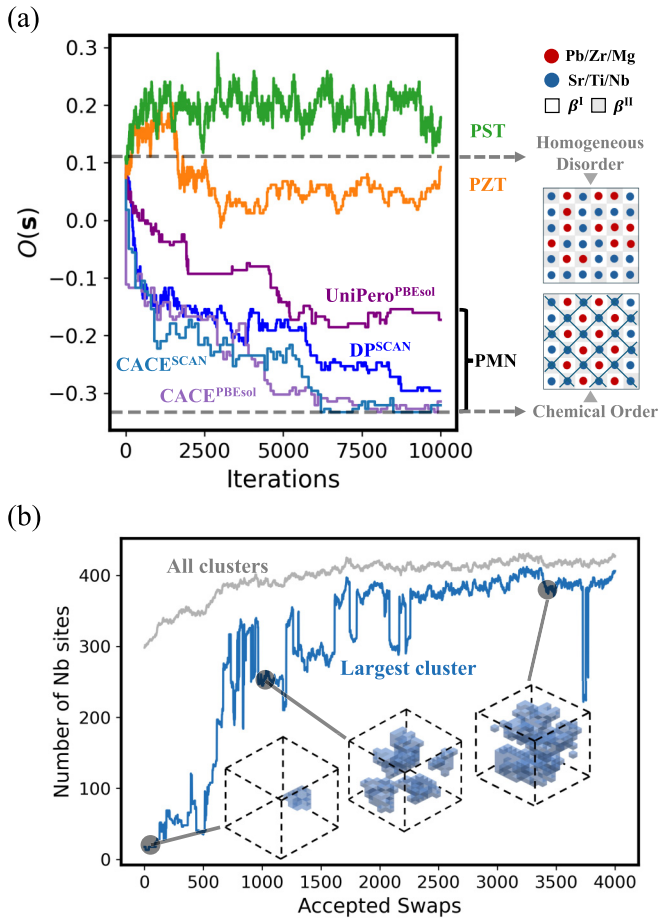


FIG. 2. (a) Order parameter $O(\mathbf{s})$ as a function of FIRE-Swap iterations on the $6 \times 6 \times 6$ supercell. The right panel illustrates cross sections of the simulation cell, corresponding to CS with homogeneous disorder (PST and PZT) and CS with a chemical order (PMN). Sublattice β^{II} is represented by gray tiles. (b) The number of Nb sites in all Nb clusters (gray) and in the largest cluster (blue). The insets show the geometry of the largest cluster in the $12 \times 12 \times 12$ lattice.

almost exclusively by Nb ions [52], whereas β^{I} contains a random 1:2 mixture of Nb and Mg ions. The second is the space-charge model [43], in which $PbNb_{1/2}Mg_{1/2}O_3$ rock-salt-ordered clusters (for brevity, rock-salt clusters) coexist with $PbNbO_3$ clusters (Nb clusters). Because both clusters carry net space charge, rock-salt clusters were postulated to be nanodomains with Nb-ion shells. Over the years, experiments have supported the existence of the Nb-rich β^{II} structure [20,43,53,54], but concrete evidence for the space-charge model remains lacking. Electrostatic considerations also disfavor the space-charge model. However, the random-site model is also incomplete: its assumption of a fully random β^{I} sublattice has not yet been confirmed and warrants reexamination.

B. Intrinsic compositional structures

Together, the four MLIPs enable a first-principles examination of the aforementioned issues and provide a strong consistency check. We first use UniPero for a comparative study of PMN, PZT, and PST, confirming that only PMN exhibits notable chemical order. We perform FIRE-Swap simulations on $6 \times 6 \times 6$ supercells of PMN, PZT, and PST at $T_{FS} = 600$ K, 300 K, and 300 K, respectively (see Appendix B for technical details). Each simulation starts from a homogeneously disordered configuration, with mixed B-site atoms (PMN and PZT) or mixed A-site atoms (PST) randomly assigned to the lattice. To track the formation of a sublattice dominated by one element, we use the order parameter $O(\mathbf{s}) = \frac{1}{6N_c}\sum_{i\sim j} s_i s_j$, where $N_c = 216$ is the total number of primitive sites and $i \sim j$ denotes all nearest-neighbor pairs of B sites (PMN and PZT) or A sites (PST). We set $s_i = 1$ for Sr, Ti, and Nb, and $s_i = -1$ otherwise. A homogeneously disordered state gives $O = 1/9$, whereas $O = -\frac{1}{3}$ corresponds to a β^{II} sublattice fully occupied by one element. All simulations equilibrate within 10^4 iterations.

Results are shown in Fig. 2(a). Indeed, O fluctuates around $1/9$ for PZT and PST, consistent with homogeneous disorder, but approaches $-\frac{1}{3}$ for PMN. All models except UniPero predict a stable O near $-\frac{1}{3}$, with cumulative ΔE_n from accepted swaps of 60–70 meV/f.u. in each case. UniPero predicts a higher equilibrium O because small Mg clusters ($PbMgO_3$ units) locally disrupt chemical order in Nb-rich β^{II}. The discrepancy between PBEsol-based CACE-LR and UniPero likely reflects missing long-range electrostatic interactions in UniPero, which effectively captures only short-range electrostatics within 6 Å [41]. This bias may facilitate Mg clustering, which should otherwise be disfavored because the average ionic charge of a $PbMgO_3$ unit is $-2e$, whereas that of a $PbNbO_3$ unit is only $+e$.

A comprehensive study of long-range electrostatics is left for future work. Within the present scope, the key result is robust: across different density functionals and MLIP architectures, FIRE-Swap reveals the Nb-rich sublattice prescribed by the random-site model, distinguishing the intrinsic CS of PMN from those of PZT and PST solid solutions. Furthermore, we perform DP-driven FIRE-Swap simulations for PMN at $T_{FS} = 1200$ K, which is comparable to experimental synthesis temperatures. We find that O fluctuates between -0.15 and $-1/3$, rather than steadily approaching $-1/3$ [23]. This deviation from $-1/3$ arises from strong thermal fluctuations that interrupt long-range chemical order, producing small chemically disordered regions. These features are consistent with STEM evidence of interrupted chemical order and antiphase boundaries [55] in PMN samples [20].

Next, FIRE-Swap simulations of a $12 \times 12 \times 12$ supercell ($N_c = 1728$) reveal larger-scale features of PMN CS, including nontrivial Nb clustering that goes beyond the random-site model. We define a Nb cluster as follows: a Nb site belongs to a cluster if it has at most one Mg-site neighbor among its six nearest neighbors. All such Nb sites form a lattice subgraph, which can be uniquely partitioned into connected components (clusters). Different clusters are disconnected on the lattice. The cluster size is the number of Nb sites in each component. For any given CS, a Breadth-First Search algorithm [56,57] computes the Nb-cluster size distribution and identifies the largest cluster. To accelerate sampling, we initialize CS according to the random-site model. The initial CS contains about 300 Nb sites distributed across roughly 250 Nb clusters.

Figure 2(b) shows results from the DP-driven simulation at $T_{FS} = 600$ K, in which about 4000 swaps are accepted over 3×10^5 iterations. The cumulative ΔE_n from accepted swaps is about 20 meV/f.u. The total number of Nb sites in all Nb clusters increases to about 430 (gray curve), close to the upper bound $N_c/3$ [58]. The largest Nb cluster grows from 17 to about 400 sites (blue curve). We find almost all clustered Nb sites collapse into a single cluster that almost percolates the lattice. Nb sites outside Nb clusters are mostly embedded in the rock-salt cluster [59] and belong to sublattice β^{II}. The chemical ordering in β^{II} is well maintained: $O(\mathbf{s})$ remains within $[-1/3, -0.3]$. Throughout the simulation, one-third of nearest-neighbor pairs are Nb–Nb, two-thirds are Nb–Mg, and less than 1% are Mg–Mg. These values agree well with x-ray-scattering statistics: 33.7% of nearest-neighbor pairs are Nb–Nb and 65.8% are Nb–Mg [19].

We identify two anomalies in Nb clustering relative to standard phase-separation behavior. First, percolation theory on β^{I} predicts a power-law cluster-size distribution, which would naively imply many more intermediate-size clusters. Second, the surface of the largest Nb cluster does not coarsen substantially [see illustrations in Fig. 2(b)]. Its surface-to-volume ratio η remains above 2 throughout the simulation, whereas a perfect cubic cluster with volume $N_c/3$ would give $\eta < 1$. The first anomaly is expected: Nb ions anchored in β^{II} strongly promote the formation of a dominant Nb cluster, rendering standard percolation arguments irrelevant. The second anomaly may arise because local interactions favor 1:1 rock-salt ordering and maximize the Nb–Mg interfacial area. As a result, the largest Nb cluster adopts a mesh-like geometry with high η, which suppresses space-charge accumulation and eliminates the need for the Nb-ion shell hypothesized in the space-charge model. The mesh-like geometry also allows both Nb clusters and rock-salt clusters to extend locally over straight segments only a few unit cells along crystalline axes [60], consistent with the experimental evidence that the globally averaged correlation length of chemical order is roughly a few unit cells [19]. These observations go beyond existing CS models and the averaged properties probed by scattering experiments, providing a detailed, first-principles mesoscale description of PMN, which we term the "anchored-mesh" model.

UniPero- and CACE-LR-driven FIRE-Swap simulations of the same PMN supercell consistently support the formation of a dominant Nb cluster [23] and the anchored-mesh model. Finite-size artifacts are also ruled out [23]. By contrast, FIRE-Swap simulations of a $12 \times 12 \times 12$ PZT supercell, the isovalent counterpart of PMN, show a lack of chemical order and numerous small Zr and Ti clusters [23].

C. Intrinsic geometric and dipolar structures

How do the anchored-mesh model and the MLIP together describe geometric and dipolar properties of PMN? We perform DP-driven NVT MD simulations of a $12 \times 12 \times 12$ PMN supercell with the optimized intrinsic CS over thermal temperatures T from 100 K to 700 K, with each run lasting 10 ns. For $T = 300$ K, we calculate the spherically symmetrized structure factor $S(Q)$ using standard neutron scattering lengths [61]. The pair distribution function $H(r) \propto r^{-1} \int_0^\infty Q(S(Q) - 1) \sin(Qr) dQ$ is plotted in Fig. 3 for comparison with measurements on PMN powder samples [62]. The overall agreement is decent. A minor but notable discrepancy appears near $r \approx 2.5$ Å, where the predicted $H(r)$ shows a small peak that is absent in the experiment. The origin of peaks in $H(r)$ is illustrated in the lower panel of Fig. 3, which reports the radial distribution function $g(r)$. We find that the small peak near $r \approx 2.5$ Å in the predicted $H(r)$ is associated with Pb-O pairs, which exhibit a broad distribution over [2.25, 3.5] Å. This is in close agreement with the broad Pb-O peaks (one at $r \approx 2.4$ Å and strengthened below room temperature) in the same interval from x-ray scattering [63]. These minor discrepancies are primarily due to errors in the density functional approximation [34], which affect bond lengths and thermal broadening. In [23], we show that both $H(r)$ and $g(r)$ are not sensitive to changes in CS [64]. The results in Fig. 3 therefore mainly serve as a consistency check with experiments, rather than as a validation of the sampled CS.

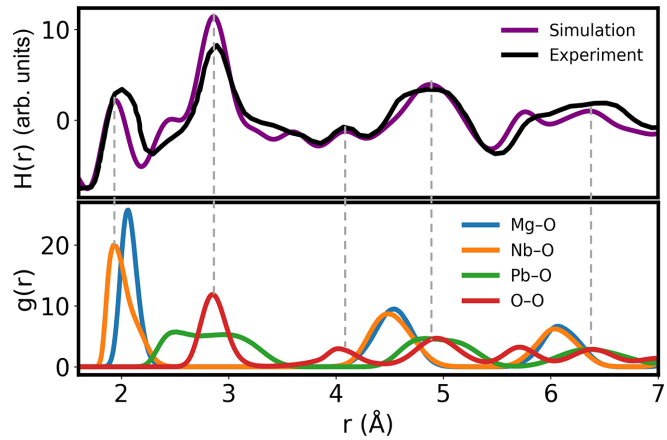


FIG. 3. Upper panel: predicted (purple) and experimental [21] (black) $H(r)$ associated with PMN powder samples at $T = 300$ K. Lower panel: the predicted radial distribution function for $T = 300$ K.

Then, we study how CS shapes local polarity in relaxors [51,54,65–68]. We characterize local polarity in PMN using the displacement $\mathbf{d}_i$ of each B-site ion i from the geometric center of its oxygen octahedral cage. $\mathbf{d}_i$ is strongly correlated with local (primitive-cell) dipole moments [69] and the softening of its vibration is a signature of ferroelectric phase transitions [9]. The displacement of the A-site Pb ion relative to neighboring oxygen ions can also describe local polarity [16,21], but it is less informative for understanding the role of chemical heterogeneity [23].

We report the temperature-dependent probability density function (PDF) of $\mathbf{d}_i$ in Fig. 4(a). The PDF $p(d_i^x, d_i^y)$ for Nb ions in Nb clusters (Nb-I), Nb ions in rock-salt clusters (Nb-II), and Mg ions is plotted separately. Overall, these PDFs show how dipolar disorder quenches as temperature decreases from 700 K to 100 K, consistent with the phenomenology of different stages of relaxor ferroelectricity [8]. Above the Burns temperature, $T_B^{EXP} \approx 620$ K [2], the PDFs for Nb-I, Nb-II, and Mg all display spherical symmetry, indicating a paraelectric state. Between T_B^{EXP} and the freezing

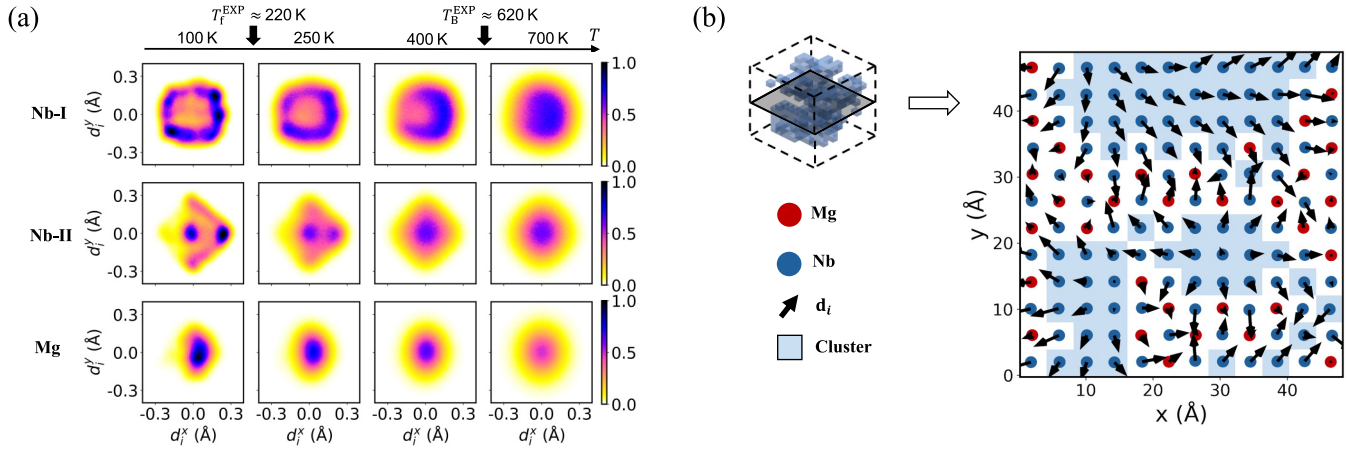


FIG. 4. (a) Histograms of PDF $p(d_i^x, d_i^y)$ associated with different types of B sites and different temperatures. The PDF $p(d_i^x, d_i^z)$ has similar features and they are omitted here. (b) (d_i^x, d_i^y) as arrows on an arbitrary perovskite layer (in the XY plane) of the simulation box. Blue shades mark Nb clusters.

temperature, $T_f^{EXP} \approx 220$ K [5], signs of quenched disorder appear in $\mathbf{d}_i$ for Nb-I and Nb-II. Below T_f^{EXP}, this disorder in Nb-I and Nb-II becomes substantially quenched (i.e., frozen), corresponding to the so-called nonergodic relaxor phase.

Notably, the behavior of $\mathbf{d}_i$ differs across different types of clusters. The PDFs associated with Mg vary much less with temperature than the others, indicating that polar fluctuations of Mg ions may play a minor role in shaping relaxor ferroelectricity. Many qualitative differences between Nb-I and Nb-II are also evident in the PDFs. Some may reflect finite-size effects caused by insufficient self-averaging, such as weak mirror-symmetry breaking (e.g., $x \to -x$) in the PDF, which is evident for $T \leqslant 250$ K. This artifact may be reduced by simulating a much larger supercell. Here, we focus on the key difference that is robust to finite-size effects and most relevant to how CS shapes relaxor ferroelectricity: at $T = 100$ K, the PDF of Nb-I exhibits a continuous distribution of disorder, whereas the PDF of Nb-II is less diffuse and shows separated peaks. This implies that Nb-II is less electrically susceptible than Nb-I because of its greater rigidity. The flexible $\mathbf{d}_i$ of Nb-I and its continuous distribution are reminiscent of polar nanoregions (PNRs), a phenomenological concept that remains debated but is widely postulated to be a key mechanism of relaxor ferroelectricity.

Here, we can examine the direct connection between CS and PNRs. In Fig. 4(b), we report a representative configuration of $\mathbf{d}_i$ using a snapshot of (d_i^x, d_i^y) on one layer (in the XY plane) of the supercell from the $T = 100$ K MD simulation. At low temperatures, the direction of $\mathbf{d}_i$ is nearly frozen against thermal fluctuations, forming PNRs within the Nb clusters marked with blue shading in Fig. 4(b). Neighboring $\mathbf{d}_i$ vectors in the Nb clusters appear strongly correlated but not rigidly aligned. Therefore, these "soft" PNRs are potentially subject to reorientation by thermal and electric perturbations on an extended time scale. We quantify dipolar correlation using the equilibrium correlation function for neighboring $\mathbf{d}_i$ and $\mathbf{d}_j$, defined as $C_{ij} = \langle \mathbf{d}_i \mathbf{d}_j \rangle / \sqrt{\langle \|\mathbf{d}_i\|^2 \rangle \langle \|\mathbf{d}_j\|^2 \rangle}$. The results are shown in Fig. 5. We found that the correlation function increases as the temperature decreases. Notably, C_{ij} for Nb pairs rises to around 0.8 at $T = 100$ K. This amounts to a correlation length of around 2 nm. Meanwhile, C_{ij} for Nb-Mg pairs that reside in rock-salt clusters has a correlation length small enough that different Nb-II sites are almost uncorrelated.

These observations suggest that the phenomenological picture of separated, frustrated nanosized PNRs [51,70] is likely imprecise. In the anchored-mesh model, intrinsic PNRs composed of correlated Nb sites are not isolated by a disordered matrix and do not behave as "mesoscopic dipoles." Instead, they form interconnected and noncoarsened dipolar structures that should be studied as a whole. This picture is independently supported by a recent STEM study of PMN [71], which reported that PNRs evolve from isolated nanoregions at room temperature into interconnected, percolating polar structures at low temperature, while chemically ordered nanoregions remain largely static and restrict PNR growth.

The lack of sharp dipolar interfaces is conceptually similar to earlier findings that some relaxors have a high density of low-angle domain walls [16]. Presumably, the dielectric responses of PMN rely on the slow evolution of these "soft" PNRs on the microsecond scale and above, leading to the unique Vogel-Fulcher law [4] that describes the

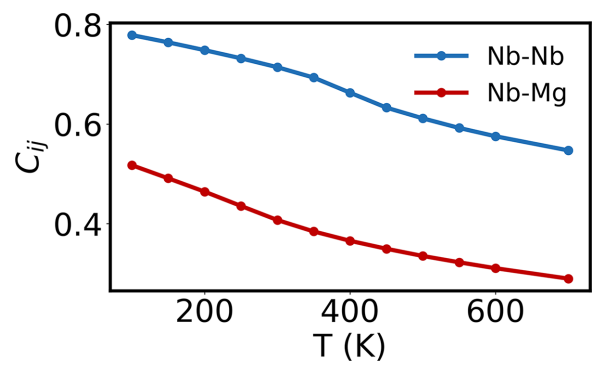


FIG. 5. Correlation functions C_{ij} (averaged over eligible pairs) for nearest-neighbor Nb-Nb pairs and Nb-Mg pairs.

frequency-dependent dielectric maximum in relaxor ferroelectrics. In principle, one can calculate the dielectric permittivity with our optimized CS, but advanced enhanced sampling methods will be necessary to bridge the large gap between the typical time scale (ps∼ns) of molecular dynamics simulations and that (ns∼s) accessible to experiments. This time scale limitation is a significant obstacle, regardless of the technical route (via the fluctuation-dissipation theorem or via finite-difference methods) employed to estimate the permittivity. We leave this for future work.

IV. CONCLUSION

We have introduced the FIRE-Swap method. By coupling chemical swaps to full geometric relaxation on machine-learned PES, the method avoids assuming random disorder, special quasirandom structures, or phenomenological ordering models. For PMN, FIRE-Swap identifies robust rock-salt-like chemical order and an anchored-mesh Nb-cluster morphology. This structure explains how intrinsic PNRs can form as interconnected, noncoarsened dipolar structures rather than isolated polar clusters. The contrast with PZT and PST shows that this mesoscale organization is intrinsic to PMN rather than a generic consequence of alloy-like disorder.

More broadly, with accurate universal MLIPs [72–74], FIRE-Swap provides a transferable workflow for future first-principles studies of complex materials with substitutional disorder. It can supply the representative CS needed before computing thermodynamic and spectroscopic properties. To facilitate this, we developed the open-source PYTHON package perostruc [75], which enables FIRE-Swap simulations with any interatomic potential models that interface with the `atomic simulation environment` [76] library.

ACKNOWLEDGMENTS

We thank R. Car and S. Liu for fruitful discussions. VASP calculations were done when P.X. and K.C. were graduate students in R. Car's group at Princeton, where the VASP license is issued. P.X. and K.C. were supported by the Computational Chemical Sciences Center: Chemistry in Solution and at Interfaces (CSI), funded by the U.S. Department of Energy (DOE) Award No. DE-SC0019394. Part of the calculations were performed using the Princeton Research Computing resources at Princeton University, which is a consortium of groups led by the Princeton Institute for Computational Science and Engineering (PICSciE) and Office of Information Technology's Research Computing. P.X. was then supported by the Alvarez Fellowship of Lawrence Berkeley National Lab. X.X. was supported by the Berkeley Lab 2025 Summer Program. X.X. and P.X. were supported by the DOE Advanced Scientific Computing Research (ASCR) Applied Mathematics program under Contract No. DE-AC02-05CH11231. P.Z. was supported by the NUS Presidential Young Professorship and the computational resources from NUS-HPC (Grant No. CFP04-CF-010). This research used resources of the National Energy Research Scientific Computing Center (NERSC), a Department of Energy User Facility, using AI4Sci@NERSC Award No. DDR-ERCAP 34636.

DATA AVAILABILITY

Data sets, models, and scripts that can reproduce the findings of this study are publicly available on GitHub [77].

APPENDIX A: DETAILS OF MLIPs

Deep potential. Our deep potential (DP) model for PMN is based on DFT with SCAN approximation [33]. The combination of DP and SCAN has also been used to model other ferroelectrics [78–80]. We use VASP [81,82] and the projector augmented wave potentials [83] for all DFT calculations. The smallest spacing between k points is 0.6 Å^{-1}. The gamma point is always included. The SCAN-DFT data set is generated using the active-learning framework DPGEN [84,85], with pressures in the interval $[1, 3 \times 10^4]$ bar and temperatures in the interval [150, 650] K. Active exploration of the configuration space is performed via NPT-MD simulations initialized from PMN configurations with different sizes and disorder patterns. Specifically, three types of initial configurations are used: (1) charge-balanced supercells of 36 PMN units (180 atoms) prescribed by the random-site model, (2) charge-balanced supercells of 72 PMN units prescribed by the random-site model, and (3) charge-balanced supercells of 27 PMN units with complete B-site disorder.

The active learning procedure consists of 15 exploration iterations. We used data from 12 iterations, together with the initial data set manually generated before active learning, as the training set, which contains DFT energy and force labels for 1386 different atomic configurations. The data from the other three iterations are used as the test set, containing 300 different atomic configurations. With the train set, we use DEEPMD-KIT [86–88] to train a DP model with a short-range cutoff 6 Å. A plot of model error distribution in the train set and the test set is provided in [23]. We find a root-mean-squared error (RMSE) of 0.8 meV/atom and 1.0 meV/atom on the train set and the test set, respectively.

CACE-LR. The CACE-LR model captures long-range electrostatic interactions through latent Ewald summation [39,40,42]. In this work, the CACE-LR model is trained for $Pb(Mg_{1/3}Nb_{2/3})_{1-x}Ti_xO_3$ solid solutions following the Pretrain-FineTune-Distillation (pfd-kit) [89] protocol. Here, the pretrained baseline model is selected as the universal DPA-3 model [90]. We use 2000 PBEsol-DFT data points to fine-tune the DPA-3 model, covering six composition ratios ($x = 0, 0.25, 0.33, 0.4, 0.5, 1.0$) and various Mg/Nb/Ti compositional structures. These data points are selected from NPT-MD (700 K) trajectories using information-entropy analysis. The fine-tuned, short-ranged DPA-3 model reaches RMSEs of 0.49 meV/atom for energy and 27 meV/Å for force. We then perform NPT-MD simulations with this DPA-3 model. We select and label 10 000 configurations from MD trajectories to construct the final PBEsol-DFT data set for CACE-LR training. The final CACE-LR model achieves accuracies of 1.15 meV/atom for energy and 40 meV/Å for force relative to DFT data.

UniPero. UniPero is built on the DPA-1 (Deep Potential with self-attention) [91] framework and trained on first-principles data of perovskites involving 14 metal elements and their solid solutions over arbitrary compositions. UniPero

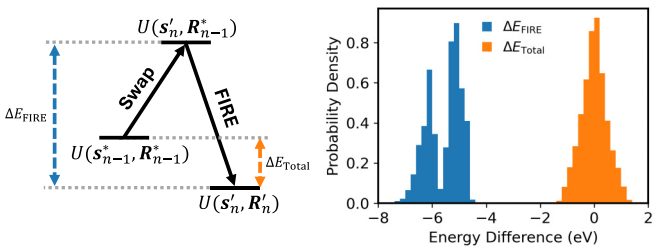


FIG. 6. Left panel: sketch of energy changes, ΔE_{FIRE} and ΔE_{Total}, in one iteration of FIRE-Swap. Right panel: the probability density distribution of ΔE_{FIRE} and ΔE_{Total} in a FIRE-Swap simulation with around 10 000 iterations.

has a short-range cutoff of 6 Å. A complete description of the training data set, data-generation workflow, DFT labeling protocol, and training errors is provided in Ref. [41], to which we refer readers for full details.

APPENDIX B: DETAILS OF FIRE-SWAP SIMULATION

PMN. The DP-driven simulations are performed with a fixed lattice constant $a = 4.05$ Å. In each FIRE relaxation, the force convergence threshold and the maximum number of optimization steps are set to $f_{\text{thr}} = 0.02$ eV/Å and $N_{\text{step}} = 100$, respectively.

The UniPero-driven simulations are performed with fixed lattice constant $a = 4.05$ Å. We use $T_{\text{FS}} = 600$ K, $f_{\text{thr}} = 0.03$ eV/Å, and $N_{\text{step}} = 100$ for the $6 \times 6 \times 6$ supercell. We use $T_{\text{FS}} = 450$ K, $f_{\text{thr}} = 0.03$ eV/Å, and $N_{\text{step}} = 50$ for the $12 \times 12 \times 12$ supercell.

The CACE-LR-driven simulations are performed with flexible cell parameters. We use $T_{\text{FS}} = 600$ K, $f_{\text{thr}} = 0.02$ eV/Å, and $N_{\text{step}} = 200$.

PZT. Simulations are performed with flexible cell parameters. We use $T_{\text{FS}} = 300$ K, $f_{\text{thr}} = 0.02$ eV/Å, and $N_{\text{step}} = 100$.

PST. Simulations are performed with flexible cell parameters and $T_{\text{FS}} = 300$ K. We use $f_{\text{thr}} = 0.03$ eV/Å and $N_{\text{step}} = 100$ for the $6 \times 6 \times 6$ supercell. We use $f_{\text{thr}} = 0.03$ eV/Å and $N_{\text{step}} = 150$ for the $12 \times 12 \times 12$ supercell.

APPENDIX C: ENERGY SCALES IN FIRE-SWAP SIMULATIONS OF PMN

Here we show that the contribution of atomic geometric disorder to system energy can be comparable to that from compositional disorder, which motivates the FIRE-Swap approach that treats compositional and geometric relaxations concurrently. We focus on two quantities: $\Delta E_{\text{FIRE}} = U(\mathbf{s}'_n, \mathbf{R}'_n) - U(\mathbf{s}'_n, \mathbf{R}^*_{n-1})$ and $\Delta E_{\text{Total}} = U(\mathbf{s}'_n, \mathbf{R}'_n) - U(\mathbf{s}^*_{n-1}, \mathbf{R}^*_{n-1})$, as indicated in the left panel of Fig. 6. The probability density distribution of ΔE_{FIRE} and ΔE_{Total} in the DP-driven FIRE-Swap simulation of a $6 \times 6 \times 6$ PMN supercell is plotted in the right panel of Fig. 6.

The distribution of ΔE_{FIRE} is associated with the energy scale relevant to atomic geometric disorder. Let $\Delta E_{\text{Swap}} = \Delta E_{\text{Total}} - \Delta E_{\text{FIRE}}$. The distribution of ΔE_{Swap} is associated with the energy scale relevant to the compositional disorder. From Fig. 6, ΔE_{FIRE} is typically around -6 eV. Meanwhile, the distribution of ΔE_{Total} resembles a zero-centered Gaussian with a standard deviation smaller than 1 eV. This suggests that the distribution of ΔE_{Swap} will be centered around 6 eV. In this case study, energy changes caused by species swapping and geometric optimization are of the same order. It is the small remnant of their cancellation that determines the acceptance of a proposed new CS.

[1] G. A. Smolensky, V. A. Isupov, A. A. Agranovskaya, and S. N. Popov, Ferroelectrics with a diffuse phase transition, Sov. Phys. Solid State **2**, 2584 (1961) [Fiz. Tverd. Tela (Leningrad) **2**, 2906 (1961)].

[2] G. Burns and F. H. Dacol, Glassy polarization behavior in ferroelectric compounds $Pb(Mg_{1/3}Nb_{2/3})O_3$ and $Pb(Zn_{1/3}Nb_{2/3})O_3$, Solid State Commun. **48**, 853 (1983).

[3] G. Burns and F. H. Dacol, Crystalline ferroelectrics with glassy polarization behavior, Phys. Rev. B **28**, 2527 (1983).

[4] D. Viehland, S. Jang, L. E. Cross, and M. Wuttig, Freezing of the polarization fluctuations in lead magnesium niobate relaxors, J. Appl. Phys. **68**, 2916 (1990).

[5] D. Viehland, M. Wuttig, and L. Cross, The glassy behavior of relaxor ferroelectrics, Ferroelectrics **120**, 71 (1991).

[6] A. Levstik, Z. Kutnjak, C. Filipič, and R. Pirc, Glassy freezing in relaxor ferroelectric lead magnesium niobate, Phys. Rev. B **57**, 11204 (1998).

[7] R. A. Cowley, S. N. Gvasaliya, S. G. Lushnikov, B. Roessli, and G. M. Rotaru, Relaxing with relaxors: A review of relaxor ferroelectrics, Adv. Phys. **60**, 229 (2011).

[8] A. A. Bokov and Z.-G. Ye, Recent progress in relaxor ferroelectrics with perovskite structure, Prog. Adv. Dielectr. **1**, 105 (2020).

[9] K. M. Rabe, C. H. Ahn, and J.-M. Triscone, *Physics of Ferroelectrics: A Modern Perspective*, Topics in Applied Physics, Vol. 105 (Springer, Berlin, 2007).

[10] D. Sherrington, BZT: A soft pseudospin glass, Phys. Rev. Lett. **111**, 227601 (2013).

[11] G. V. Lecomte, H. v. Löhneysen, and E. F. Wassermann, Frequency dependent magnetic susceptibility and spin glass freezing inPtMn alloys, Z. Phys. B **50**, 239 (1983).

[12] D. A. Porter and K. E. Easterling, *Phase Transformations in Metals and Alloys (Revised Reprint)* (CRC Press, Boca Raton, FL, 2009).

[13] See Appendix C for further discussion.

[14] W. Zhong, D. Vanderbilt, and K. M. Rabe, First-principles theory of ferroelectric phase transitions for perovskites: The case of $BaTiO_3$, Phys. Rev. B **52**, 6301 (1995).

[15] Y.-H. Shin, V. R. Cooper, I. Grinberg, and A. M. Rappe, Development of a bond-valence molecular-dynamics model for complex oxides, Phys. Rev. B **71**, 054104 (2005).

[16] H. Takenaka, I. Grinberg, S. Liu, and A. M. Rappe, Slush-like polar structures in single-crystal relaxors, Nature (London) **546**, 391 (2017).

[17] A. R. Akbarzadeh, S. Prosandeev, E. J. Walter, A. Al-Barakaty, and L. Bellaiche, Finite-temperature properties of $Ba(Zr,Ti)O_3$

relaxors from first principles, Phys. Rev. Lett. **108**, 257601 (2012).

[18] J. Zhang, L. Liu, A. A. Bokov, N. Zhang, D. Wang, Z.-G. Ye, and C.-L. Jia, Compositional ordering in relaxor ferroelectric $Pb(BB')O_3$: Nearest-neighbor approach, Phys. Rev. B **103**, 054201 (2021).

[19] M. Kopecký, J. Kub, J. Fábry, and J. Hlinka, Nanometer-range atomic order directly recovered from resonant diffuse scattering, Phys. Rev. B **93**, 054202 (2016).

[20] M. J. Cabral, S. Zhang, E. C. Dickey, and J. M. LeBeau, Gradient chemical order in the relaxor $Pb(Mg_{1/3}Nb_{2/3})O_3$, Appl. Phys. Lett. **112**, 082901 (2018).

[21] M. Eremenko, V. Krayzman, A. Bosak, H. Y. Playford, K. W. Chapman, J. C. Woicik, B. Ravel, and I. Levin, Local atomic order and hierarchical polar nanoregions in a classical relaxor ferroelectric, Nat. Commun. **10**, 2728 (2019).

[22] S. Pennycook and L. Boatner, Chemically sensitive structure-imaging with a scanning transmission electron microscope, Nature (London) **336**, 565 (1988).

[23] See Supplemental Material at http://link.aps.org/supplemental/10.1103/fz5h-1t5b for details on (1) fire-swap simulations of pmn close to the melting temperature, (2) evolution of cluster size in fire-swap simulations of PMN, PZT, and PST, (3) finite size analysis (3) pair and radial distribution functions associated to different compositional structures, (4) distribution of Pb-based local order parameter, and (5) error distribution of deep potential model.

[24] E. C. Neyts and A. Bogaerts, Combining molecular dynamics with Monte Carlo simulations: Implementations and applications, Theor. Chem. Acc. **132**, 1320 (2013).

[25] M. Widom, W. P. Huhn, S. Maiti, and W. Steurer, Hybrid Monte Carlo/molecular dynamics simulation of a refractory metal high entropy alloy, Metall. Mater. Trans. A **45**, 196 (2014).

[26] E. Antillon, C. Woodward, S. Rao, B. Akdim, and T. Parthasarathy, Chemical short range order strengthening in a model fcc high entropy alloy, Acta Mater. **190**, 29 (2020).

[27] E. Bitzek, P. Koskinen, F. Gähler, M. Moseler, and P. Gumbsch, Structural relaxation made simple, Phys. Rev. Lett. **97**, 170201 (2006).

[28] F. H. Stillinger and T. A. Weber, Inherent structure in water, J. Phys. Chem. **87**, 2833 (1983).

[29] D. S. Corti, P. G. Debenedetti, S. Sastry, and F. H. Stillinger, Constraints, metastability, and inherent structures in liquids, Phys. Rev. E **55**, 5522 (1997).

[30] N. Nakagawa and M. Peyrard, The inherent structure landscape of a protein, Proc. Natl. Acad. Sci. USA **103**, 5279 (2006).

[31] The mixing ratios of PZT and PST are chosen to match PMN's Mg:Nb ratio, allowing PZT and PST to serve as isovalent control systems. This isolates whether FIRE-Swap predicts chemical order specifically due to PMN's heterovalent chemistry, rather than the mixing ratio itself.

[32] J. P. Perdew, A. Ruzsinszky, G. I. Csonka, O. A. Vydrov, G. E. Scuseria, L. A. Constantin, X. Zhou, and K. Burke, Restoring the density-gradient expansion for exchange in solids and surfaces, Phys. Rev. Lett. **100**, 136406 (2008).

[33] J. Sun, A. Ruzsinszky, and J. P. Perdew, Strongly constrained and appropriately normed semilocal density functional, Phys. Rev. Lett. **115**, 036402 (2015).

[34] Y. Zhang, J. Sun, J. P. Perdew, and X. Wu, Comparative first-principles studies of prototypical ferroelectric materials by LDA, GGA, and SCAN meta-GGA, Phys. Rev. B **96**, 035143 (2017).

[35] J. Han, L. Zhang, R. Car, and W. E, Deep potential: A general representation of a many-body potential energy surface, Commun. Comput. Phys. **23**, 629 (2025).

[36] L. Zhang, J. Han, H. Wang, R. Car, and W. E, Deep potential molecular dynamics: A scalable model with the accuracy of quantum mechanics, Phys. Rev. Lett. **120**, 143001 (2018).

[37] L. Zhang, J. Han, H. Wang, W. A. Saidi, R. Car, *et al.*, End-to-end symmetry preserving inter-atomic potential energy model for finite and extended systems, in *Advances in Neural Information Processing Systems* (Curran Associates, Red Hook, NY, 2018), Vol. 31.

[38] B. Cheng, Cartesian atomic cluster expansion for machine learning interatomic potentials, npj Comput. Mater. **10**, 157 (2024).

[39] D. S. King, D. Kim, P. Zhong, and B. Cheng, Machine learning of charges and long-range interactions from energies and forces, Nat. Commun. **16**, 8763 (2025).

[40] P. Zhong, D. Kim, D. S. King, and B. Cheng, Machine learning interatomic potential can infer electrical response, npj Comput. Mater. **11**, 384 (2025).

[41] J. Wu, J. Yang, Y.-J. Liu, D. Zhang, Y. Yang, Y. Zhang, L. Zhang, and S. Liu, Universal interatomic potential for perovskite oxides, Phys. Rev. B **108**, L180104 (2023).

[42] B. Cheng, Latent Ewald summation for machine learning of long-range interactions, npj Comput. Mater. **11**, 80 (2025).

[43] J. Chen, H. M. Chan, and M. P. Harmer, Glassy polarization behavior in ferroelectric compounds $Pb(Mg_{1/3}Nb_{2/3})O_3$ and $Pb(Zn_{1/3}Nb_{2/3})O_3$, J. Am. Ceram. Soc. **72**, 593 (1989).

[44] C. A. Randall, A. S. Bhalla, T. R. Shrout, and L. E. Cross, Classification and consequences of complex lead perovskite ferroelectrics with regard to B-site cation order, J. Mater. Res. **5**, 829 (1990).

[45] C. Boulesteix, F. Varnier, A. Llebaria, and E. Husson, Numerical determination of the local ordering of $Pb(Mg)_{1/3}Nb_{2/3}O_3$ (PMN) from high-resolution electron microscopy images, J. Solid State Chem. **108**, 141 (1994).

[46] Z. Kutnjak, C. Filipič, R. Pirc, A. Levstik, R. Farhi, and M. El Marssi, Slow dynamics and ergodicity breaking in a lanthanum-modified lead zirconate titanate relaxor system, Phys. Rev. B **59**, 294 (1999).

[47] P. Davies and M. Akbas, Chemical order in PMN-related relaxors: Structure, stability, modification, and impact on properties, J. Phys. Chem. Solids **61**, 159 (2000).

[48] M. A. Akbas and P. K. Davies, Thermally induced coarsening of the chemically ordered domains in $Pb(Mg_{1/3}Nb_{2/3})O_3$ (PMN)-based relaxor ferroelectrics, J. Am. Ceram. Soc. **83**, 119 (2000).

[49] Z. Xu, S. M. Gupta, D. Viehland, Y. Yan, and S. J. Pennycook, Direct imaging of atomic ordering in undoped and La-doped $Pb(Mg_{1/3}Nb_{2/3})O_3$, J. Am. Ceram. Soc. **83**, 181 (2000).

[50] L. Farber and P. K. Davies, Influence of cation order on the dielectric properties of $Pb(Mg_{1/3}Nb_{2/3})O_3$–$Pb(Sc_{1/2}Nb_{1/2})O_3$ (PMN–PSN) relaxor ferroelectrics, J. Am. Ceram. Soc. **86**, 1861 (2003).

[51] D. Fu, H. Taniguchi, M. Itoh, S. y. Koshihara, N. Yamamoto, and S. Mori, Relaxor $Pb(Mg_{1/3}Nb_{2/3})O_3$: A ferroelectric with multiple inhomogeneities, Phys. Rev. Lett. **103**, 207601 (2009).

[52] The formation of Nb-rich sublattice prevents the adjacency of the Mg sites that presumably contribute to greater electrostatic repulsion than the adjacent Mg-Nb and Nb-Nb sites.
[53] M. Cantoni, S. Bharadwaja, S. Gentil, and N. Setter, Direct observation of the B-site cationic order in the ferroelectric relaxor $Pb(Mg_{1/3}Ta_{2/3})O_3$, J. Appl. Phys. **96**, 3870 (2004).
[54] A. Kumar, J. N. Baker, P. C. Bowes, M. J. Cabral, S. Zhang, E. C. Dickey, D. L. Irving, and J. M. LeBeau, Atomic-resolution electron microscopy of nanoscale local structure in lead-based relaxor ferroelectrics, Nat. Mater. **20**, 62 (2021).
[55] Antiphase boundaries are disordered regions where the $\beta^{\mathrm{I/II}}$ classification flips.
[56] E. F. Moore, The shortest path through a maze, in *Proceedings of the International Symposium on the Theory of Switching* (Harvard University Press, Cambridge, MA, 1959), pp. 285–292.
[57] C. Y. Lee, An algorithm for path connections and its applications, IRE Trans. Electron. Comput. **EC-10**, 346 (1961).
[58] The upper bound corresponds to the maximal separation between Nb clusters and rock-salt clusters. The upper bound cannot be reached because our definition of a Nb cluster omits sites at the interface.
[59] We verify this by tracking the number of Nb sites in the rock-salt cluster, where an Nb site belongs to the rock-salt cluster if it has at most one Nb neighbor. Details are omitted here but are available in the Supplemental Data and Code [77].
[60] Visualization is provided later in Fig. 4(b).
[61] Pb: 9.405 fm; Mg: -3.73 fm; Nb: 7.054 fm; O: 5.803 fm.
[62] See Supplemental Fig. 1 of Ref. [21].
[63] See Supplemental Fig. 17(a) of Ref. [21].
[64] This highlights potential nonuniqueness in CS inferred from reverse Monte Carlo methods.
[65] S. Wakimoto, C. Stock, R. J. Birgeneau, Z.-G. Ye, W. Chen, W. J. L. Buyers, P. M. Gehring, and G. Shirane, Ferroelectric ordering in the relaxor $Pb(Mg_{1/3}Nb_{2/3})O_3$ as evidenced by low-temperature phonon anomalies, Phys. Rev. B **65**, 172105 (2002).
[66] R. Blinc, V. V. Laguta, and B. Zalar, Field-cooled and zero-field-cooled ^{207}Pb NMR and the local structure of relaxor $Pb(Mg_{1/3}Nb_{2/3})O_3$, Phys. Rev. Lett. **91**, 247601 (2003).
[67] I.-K. Jeong, T. W. Darling, J. K. Lee, T. Proffen, R. H. Heffner, J. S. Park, K. S. Hong, W. Dmowski, and T. Egami, Direct observation of the formation of polar nanoregions in $Pb(Mg_{1/3}Nb_{2/3})O_3$ using neutron pair distribution function analysis, Phys. Rev. Lett. **94**, 147602 (2005).
[68] P. M. Gehring, H. Hiraka, C. Stock, S.-H. Lee, W. Chen, Z.-G. Ye, S. B. Vakhrushev, and Z. Chowdhuri, Reassessment of the Burns temperature and its relationship to the diffuse scattering, lattice dynamics, and thermal expansion in relaxor $Pb(Mg_{1/3}Nb_{2/3})O_3$, Phys. Rev. B **79**, 224109 (2009).
[69] The local dipole moment can be rigorously defined from the Wannier-center representation of polarization prescribed by Berry-phase theory [92,93], as in Ref. [79].
[70] D. Fu, H. Taniguchi, M. Itoh, and S. Mori, $Pb(Mg_{1/3}Nb_{2/3})O_3$ (PMN) relaxor: Dipole glass or nano-domain ferroelectric? in *Advances in Ferroelectrics* (IntechOpen, London, 2012).
[71] K. Hino, D. Morikawa, D. Fu, M. Itoh, and K. Tsuda, Direct imaging of temperature evolution of polar nanoregions and chemically ordered regions in PMN relaxor: Evidence for polar phase percolation, Appl. Phys. Lett. **128**, 142901 (2026).
[72] B. Deng, P. Zhong, K. Jun, J. Riebesell, K. Han, C. J. Bartel, and G. Ceder, Chgnet as a pretrained universal neural network potential for charge-informed atomistic modelling, Nat. Mach. Intell. **5**, 1031 (2023).
[73] D. Zhang, X. Liu, X. Zhang, C. Zhang, C. Cai, H. Bi, Y. Du, X. Qin, A. Peng, J. Huang, *et al.*, DPA-2: A large atomic model as a multi-task learner, npj Comput. Mater. **10**, 293 (2024).
[74] I. Batatia, P. Benner, Y. Chiang, A. M. Elena, D. P. Kovács, J. Riebesell, X. R. Advincula, M. Asta, M. Avaylon, W. J. Baldwin, *et al.*, A foundation model for atomistic materials chemistry, J. Chem. Phys. **163**, 184110 (2025).
[75] PeroStruc, https://github.com/Kehan-Cai-nanako/PeroStruc.
[76] A. Hjorth Larsen, J. Jørgen Mortensen, J. Blomqvist, I. E. Castelli, R. Christensen, M. Dułak, J. Friis, M. N. Groves, B. Hammer, C. Hargus, *et al.*, The atomic simulation environment—A python library for working with atoms, J. Phys.: Condens. Matter **29**, 273002 (2017).
[77] Supplemental data and code, https://github.com/xuxinyu2820/PMN_COR.
[78] B. Yang, P. Xie, and R. Car, Deuteration removes quantum dipolar defects from KDP crystals, npj Comput. Mater. **10**, 241 (2024).
[79] P. Xie, Y. Chen, W. E, and R. Car, Thermal disorder and phonon softening in the ferroelectric phase transition of lead titanate, Phys. Rev. B **111**, 094113 (2025).
[80] P. Xie, Y. Chen, X. Xu, Z. Yao, W. E, and R. Car, *Ab initio* bulk free energy surface of proper ferroelectrics, Phys. Rev. Lett. **136**, 056801 (2026).
[81] G. Kresse and J. Furthmüller, Efficient iterative schemes for *ab initio* total-energy calculations using a plane-wave basis set, Phys. Rev. B **54**, 11169 (1996).
[82] G. Kresse and J. Furthmüller, Efficiency of *ab-initio* total energy calculations for metals and semiconductors using a plane-wave basis set, Comput. Mater. Sci. **6**, 15 (1996).
[83] G. Kresse and D. Joubert, From ultrasoft pseudopotentials to the projector augmented-wave method, Phys. Rev. B **59**, 1758 (1999).
[84] L. Zhang, D.-Y. Lin, H. Wang, R. Car, and W. E, Active learning of uniformly accurate interatomic potentials for materials simulation, Phys. Rev. Mater. **3**, 023804 (2019).
[85] Y. Zhang, H. Wang, W. Chen, J. Zeng, L. Zhang, H. Wang, and W. E, DP-GEN: A concurrent learning platform for the generation of reliable deep learning based potential energy models, Comput. Phys. Commun. **253**, 107206 (2020).
[86] H. Wang, L. Zhang, J. Han, and W. E, DeePMD-kit: A deep learning package for many-body potential energy representation and molecular dynamics, Comput. Phys. Commun. **228**, 178 (2018).
[87] D. Lu, H. Wang, M. Chen, L. Lin, R. Car, W. E, W. Jia, and L. Zhang, 86 PFLOPS deep potential molecular dynamics simulation of 100 million atoms with *ab initio* accuracy, Comput. Phys. Commun. **259**, 107624 (2021).
[88] J. Zeng, D. Zhang, D. Lu, P. Mo, L. Zhang, H. Wang, W. E, R. Car, *et al.*, DeePMD-kit v2: A software package for deep potential models, J. Chem. Phys. **159**, 054801 (2023).

[89] R. Wang, Y. Gao, H. Wu, and Z. Zhong, Pre-training, fine-tuning, and distillation (PFD): Automatically generating machine learning force fields from universal models, Phys. Rev. Mater. **9**, 113802 (2025).

[90] D. Zhang, A. Peng, C. Cai, W. Li, Y. Zhou, J. Zeng, M. Guo, C. Zhang, B. Li, H. Jiang, *et al.*, A graph neural network for the era of large atomistic models, arXiv:2506.01686.

[91] D. Zhang, H. Bi, F.-Z. Dai, W. Jiang, X. Liu, L. Zhang, and H. Wang, Pretraining of attention-based deep learning potential model for molecular simulation, npj Comput. Mater. **10**, 94 (2024).

[92] R. Resta and D. Vanderbilt, Theory of polarization: A modern approach, in *Physics of Ferroelectrics: A Modern Perspective* (Springer, Berlin, Heidelberg, 2007), pp. 31–68.

[93] N. Marzari, A. A. Mostofi, J. R. Yates, I. Souza, and D. Vanderbilt, Maximally localized Wannier functions: Theory and applications, Rev. Mod. Phys. **84**, 1419 (2012).